Motion-defined contour processing in the early visual cortex

Amol Gharat and Curtis L. Baker, Jr.

You might find this additional info useful...

This article cites 58 articles, 23 of which you can access for free at:
http://jn.physiology.org/content/108/5/1228.full#ref-list-1

Updated information and services including high resolution figures, can be found at:
http://jn.physiology.org/content/108/5/1228.full

Additional material and information about *Journal of Neurophysiology* can be found at:
http://www.the-aps.org/publications/jn

This information is current as of September 2, 2012.

Motion-defined contour processing in the early visual cortex

Amol Gharat[1] and Curtis L. Baker Jr.[2]

[1]*Department of Psychology, McGill University, Montreal, Quebec, Canada; and* [2]*McGill Vision Research Unit, Department of Ophthalmology, McGill University, Montreal, Quebec, Canada*

Gharat A, Baker CL Jr. Motion-defined contour processing in the early visual cortex. *J Neurophysiol* 108: 1228–1243, 2012. First published June 6, 2012; doi:10.1152/jn.00840.2011.—From our daily experience, it is very clear that relative motion cues can contribute to correctly identifying object boundaries and perceiving depth. Motion-defined contours are not only generated by the motion of objects in a scene but also by the movement of an observer's head and body (motion parallax). However, the neural mechanism involved in detecting these contours is still unknown. To explore this mechanism, we extracellularly recorded visual responses of area 18 neurons in anesthetized and paralyzed cats. The goal of this study was to determine if motion-defined contours could be detected by neurons that have been previously shown to detect luminance-, texture-, and contrast-defined contours cue invariantly. Motion-defined contour stimuli were generated by modulating the velocity of high spatial frequency sinusoidal luminance gratings (carrier gratings) by a moving squarewave envelope. The carrier gratings were outside the luminance passband of a neuron, such that presence of the carrier alone within the receptive field did not elicit a response. Most neurons that responded to contrast-defined contours also responded to motion-defined contours. The orientation and direction selectivity of these neurons for motion-defined contours was similar to that of luminance gratings. A given neuron also exhibited similar selectivity for the spatial frequency of the carrier gratings of contrast- and motion-defined contours. These results suggest that different second-order contours are detected in a form-cue invariant manner, through a common neural mechanism in area 18.

figure-ground segregation; second-order motion; relative motion

NATURAL SCENES abundantly contain local variations in luminance that facilitate figure-ground segregation. However, these first-order cues often introduce ambiguities and make figure-ground segregation a difficult task (Marr 1982). For example, shadows introduce false luminance boundaries that do not correspond to objects' boundaries in a visual scene. However, our visual system is able to distinguish these false boundaries from real ones using other cues, including second-order information such as texture, contrast, color, or motion differences between an object and its background. Particularly, relative motion is a powerful cue that can break camouflage when an object and its background have similar luminance, color, and texture. It can be sufficient to support perception of shape and size of three-dimensional surfaces and for depth ordering (Rogers and Graham 1979; Regan 1989; Regan and Hamstra 1992). This cue arises from motion parallax generated by an observer's movement or from the exogenous movement of objects in a scene.

Even though psychophysical studies have demonstrated the importance of relative motion cues in figure-ground segregation, the neural mechanism to detect these motion-defined boundaries is still unknown. Single-unit recording experiments by Hubel and Wiesel (1962) on cats showed that orientation selectivity for luminance edges first originates in brain areas as early as the primary visual cortex (V1). Simple cells in V1 have receptive fields with elongated excitatory and inhibitory areas lying adjacent and parallel to one another, which act as filters that perform linear summation of light intensity in their receptive fields. Hubel and Wiesel (1962) proposed a model in which receptive fields of simple cells are constructed by inputs from on-center and off-center lateral geniculate nucleus (LGN) cells arranged in alternating columns. A similar question could be asked in the case of motion-defined boundaries, i.e., where does orientation selectivity for these boundaries originate and what is the neural mechanism behind it?

Several single-unit studies have tried to locate the brain areas responsive to motion-defined boundaries and understand the underlying neural mechanism. Using temporal texture bars (dynamic random dot patterns moving on a stationary random dot background), Albright (1992) reported that most of the neurons in the area middle temporal (MT) of macaque monkeys were selective for the orientation of these bars, and Chaudhuri et al. (1997) found that more than half of the neurons in the V1 area of macaque monkeys were selective for the orientation of these bars. Marcar et al. (2000) also found a small fraction of neurons in macaque V1 and V2 that were selective for the orientations of motion-defined boundaries. In macaque V4, Mysore et al. (2006) reported a sizeable fraction of neurons (10–20%) that were selective for kinetic patterns. Both these studies (Marcar et al. 2000 and Mysore et al. 2006) used moving random dot texture patterns to generate motion-defined boundaries that were held stationary in the receptive field of a neuron. Zeki et al. (2003) found that the majority of neurons in macaque V3 and V3A were selective to the orientation of motion-defined bars made of random dot texture patterns. These studies suggest that motion-defined boundary selective neurons are present in different visual areas such as the V1, V2, V3, V3A, V4, and MT, with higher cortical areas containing a greater percentage of such cells. However, there is a potential problem with the random dot texture patterns used in all these studies, because such textures contain a broad range of spatial frequencies. Hence, these texture patterns will contain energy within the luminance passband of a neuron, and, therefore, the response of a neuron could be due to local luminance (first order) signals and not motion difference (second order) cues. Such luminance signals or artifacts can be avoided by using a sinusoidal grating as a texture pattern, with

the spatial frequency higher than the neuron's luminance resolution.

A neuroimaging study in human subjects (Reppas et al. 1997) found strong motion boundary-selective signals in early cortical areas (V1 and V2). However, it is unclear from neuroimaging studies whether the neurons in brain areas that respond to motion boundary stimuli are selective for the orientation of these boundaries, as neurons could be responding due to a center-surround antagonistic mechanism (Born and Tootell 1992; Born 2000; Shen et al. 2007) or just to the local motion of the carrier. However, a recent study (Larsson et al. 2010) was able to demonstrate orientation selectivity to motion boundaries in the human visual cortex using an event-related functional MRI adaptation technique. They showed that most of the motion boundary responsive visual areas, such as V2, V3, V3A, V3B, LO1, LO2, hV4, and V7, identified in previous neuroimaging studies (Dupont et al. 1997; Larsson and Heeger 2006; Tyler et al. 2006; Van Oostende et al. 1997; Zeki et al. 2003) are orientation selective. These results argue against the initial notion from neuroimaging studies (Dupont et al. 1997; Van Oostende et al. 1997) that motion boundaries are processed in a specialized "kinetic occipital" brain area (corresponding to LO1, LO2, and V3B).

Neuronal responses to contrast-defined (second order) boundaries have been extensively studied in cat area 18 using single-unit recordings (Zhou and Baker 1993, 1996; Mareschal and Baker 1998a, 1998a, 1999). The contrast-defined bound-aries used in these studies were constructed by a coarse spatial scale contrast pattern (envelope), which modulates the contrast of a high spatial frequency sinusoidal grating (carrier; Fig. 1B). Around half of the neurons in area 18 responded to contrast-defined boundaries in a form-cue invariant manner, i.e., they were tuned to the same orientation and motion direction of luminance (first order; Fig. 1A) and contrast-defined (second order) boundaries. In these studies, carrier spatial frequency was constrained to lie outside a neuron's spatial frequency passband (measured using luminance grating) to ensure that the response of a neuron was genuinely second order and not due to first-order luminance signals. Surprisingly, these neurons showed narrow band-pass tuning for carrier spatial frequency. Song and Baker (2007) subsequently showed that these contrast-defined boundary-responsive neurons also respond to texture-defined boundaries (second order) and again in a form-cue invariant manner. Texture-defined boundaries [illusory contours (ICs)], similar to contrast-defined boundaries, were constructed using high spatial frequency sinusoidal gratings as a carrier, whose phase was modulated by a square-wave envelope. Neurons showed narrow band-pass tuning for carrier spatial frequency of texture-defined boundaries and were selective for similar carrier spatial frequencies. These results suggest that these neurons would be functionally useful in mediating responses to boundaries regardless of the cue that defines them, and this cue invariance to different second-order boundaries might arise from a common nonlinear neuronal mechanism.
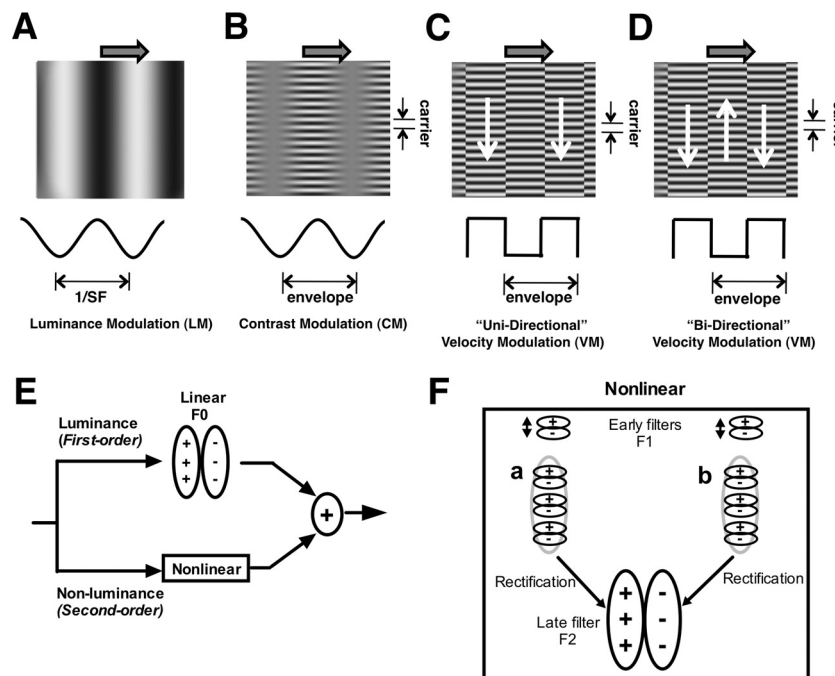

Fig. 1. The four types of grating stimuli used in this study and a model. A: luminance modulation (LM) sinusoidal grating with a vertical orientation. B: contrast modulation (CM) grating with a vertically oriented sinusoidal envelope that modulates the contrast of a horizontal high spatial frequency (SF) carrier grating. C: "uni-directional" velocity modulation (VM) grating with a vertically oriented square-wave envelope that modulates the velocity of a horizontal high SF carrier grating. For unidirectional VM, the carrier in half of the envelope cycles is stationary and in the other half drifts with a specified temporal frequency (TF). D: "bidirectional" VM grating is constructed similarly to unidirectional VM except that the carrier in alternate half-cycles of the envelope drifts with equal speeds but in opposite directions. In the stimulus images here and in the following figures, carrier motion is indicated by thin white arrows, whereas envelope motion is depicted by thick gray arrows. E: schematic model for neuronal responses, in which first- and second-order responses are mediated by separate, parallel pathways. The *top* pathway is a coarse spatial scale linear filter (F_0) that would be responsive to conventional LM gratings. The *bottom* pathway mediates nonlinear processing of CM and VM gratings. F: nonlinear filter-rectify-filter (FRF) model that responds selectively to CM and VM gratings. The first stage of the model consists of small scale filters (F_1) that are selective for high SF carriers. The outputs of these F_1 filters are rectified and pooled by a late coarse scale filter (F_2), which would be selective for the envelope of CM and VM gratings and would have similar spatiotemporal properties as the F_0 filter.

First- and second-order information are thought to be processed by two parallel pathways, based on results from both psychophysics (Ledgeway and Smith 1994; Mather and West 1993; Nishida et al. 1997; Scott-Samuel and Georgeson 1999; Allard and Faubert 2007) and neurophysiology (Zhou and Baker 1993) (for a review, see Baker and Mareschal 2001). First-order information can be detected by neurons acting as quasilinear spatiotemporal filters. To detect second-order information, neurophysiology experiments support a two-stage filter-rectify-filter (FRF) model (Mareshcal and Baker 1999), involving early filtering, which is selective for local texture characteristics, followed by rectification, and second-stage coarse-scale spatiotemporal direction selective filtering (Chubb and Sperling 1988; Wilson 1999; Landy and Graham 2004). The second-stage filter has similar properties as the first-order filter, but it pools across a coarser spatial scale. These two parallel pathways converge onto a single neuron. This model has been supported by recent optical imaging (Zhan and Baker 2006) and single-unit neurophysiology (Song and Baker 2007).

In this study, we hypothesized that second-order-responsive neurons in area 18 might also respond selectively to motion-defined boundaries and that they might do so in a form-cue invariant manner. We used high spatial frequency sinusoidal gratings as texture (carrier) patterns and the relative motion between these textures to create motion-defined boundaries (Fig. 1, *C* and *D*). To ensure that responses were not simply due to the carrier motion, we carefully optimized the spatial frequency of the carrier grating for each neuron, such that it was well outside of the neuron's conventional luminance grating resolution. A common motion-defined boundary occurs when an object moves in the visual field. In this case, the retinal image of the background is nearly stationary, but the image of the object moves; we mimicked this situation with a square-wave envelope in which alternate half-cycles contained either a moving or a stationary texture (carrier; Fig. 1*C*): a "unidirectional" motion boundary. We mimicked motion boundaries generated from motion parallax with a stimulus in which texture in alternate half-cycles of the envelope moved in opposite directions (Fig. 1*D*): a "bidirectional" motion boundary. We restricted this study to "shear" motion boundaries, in which local motions are parallel to the edge, to avoid complexities of accretion-deletion cues (Sary et al. 1994). To assess form-cue invariance, we compared neurons' responses to motion-defined boundaries with those to contrast- and luminance-defined boundaries. For all three types of boundaries, the envelope was drifting at a low temporal frequency. These comparisons also enabled inferences regarding similarity between underlying neural mechanisms for these different stimuli. In addition, we simulated a model of a generic area 18 neuron receiving inputs from two parallel pathways that separately process first- and second-order information, as described above, to see whether the selectivity of neurons to contrast- and motion-defined boundaries can be explained by a single such model.

We found that all contrast-defined boundary-responsive neurons also responded to unidirectional motion boundaries in a form-cue invariant manner and with similar carrier spatial frequency tuning. Some, but not all, contrast-defined boundary-responsive neurons also responded to bidirectional motion boundaries, typically with weaker responses than to unidirectional boundaries. The pattern of selectivity of these neurons matched well with the selectivity of the simulated model. This

suggests that motion-defined boundaries are processed by the same nonlinear neural mechanism that processes contrast-defined boundaries.

MATERIALS AND METHODS

Animal preparation. All experimental procedures were reviewed and approved by the Animal Care Committee of McGill University. Cats were anesthetized using isoflurane-oxygen and maintained with isoflurane inhalation. Methylcellulose gel (1%) was applied to protect the corneas, and a rectal thermistor inserted to monitor temperature during surgery. Intravenous cannulation was performed, and a loading dose of propofol (5 mg/kg) was delivered and then maintained at 6 $mg \cdot kg^{-1} \cdot h^{-1}$ for subsequent surgery. ECG leads were connected to monitor heart rate. Tracheal intubation was performed to provide a secure airway, and the animal was secured on a stereotaxic apparatus. A respirator (Ugo Basile) was connected to deliver a mixture of O_2-N_2O (30:70 ratio). End-tidal CO_2 was monitored with a capnometer (Hewlett-Packard) and maintained between 28 and 36 mmHg by adjusting the respirator stroke volume. A pulse-oximeter sensor (Nonin) measured blood oxygen. Eye drops [atrophine (1%) and phenylephrine (2.5%)] were applied, and neutral contact lenses were inserted. A craniotomy was made to expose area 18 [Horseley-Clarke A3/L4 (Tusa et al. 1979)] as well as a duratomy when recordings were made with multielectrodes. The craniotomy was covered with 2% agarose followed by petroleum jelly. All surgical wounds were infused with bupivacaine (0.5%), and temperature was thermostatically regulated (Harvard Apparatus) at 37.5°C. The animal was anesthetized and paralyzed with a continuous infusion of propofol (5.3 $mg \cdot kg^{-1} \cdot h^{-1}$), fentanyl (7.4 $\mu g \cdot kg^{-1} \cdot h^{-1}$), and gallamine triethiodide (10 $mg \cdot kg^{-1} \cdot h^{-1}$). Glycopyrrolate (0.005 mg/kg) and dexamethasone (0.6 mg) were delivered intramuscularly every 12 h throughout the experiment. Artificial pupils were positioned, and the appropriate spectacle lenses were selected using a slit retinoscope to provide refraction at a viewing distance of 57 cm. The optic disk was back projected on a tangent screen (Fernald and Chase 1971) and used to estimate the location of the area centralis of each eye (Nikara et al. 1968).

Visual stimuli. Visual stimuli were generated by a Macintosh (Intel 4x2.66 GHz, 6GB, NVIDIA GeForce GT 120) using Matlab with Psychophysics Toolbox (Brainard 1997; Pelli 1997) and presented on a gamma-corrected 17-in. CRT monitor (resolution: 640 × 480 pixels, 75 Hz). Stimuli were confined within 480 × 480 pixels, corresponding to 30 × 30° at a viewing distance of 57 cm. Conventional luminance modulation (LM) sine-wave gratings (Fig. 1*A*) with a contrast of 30% were used to measure the luminance passband of a neuron (spatial frequency, orientation, and temporal frequency tuning). Contrast modulation (CM) gratings (Fig. 1*B*) were constructed by modulating the contrast of a carrier (texture pattern) by a low spatial frequency grating of 100% modulation depth (envelope). The CM grating was drifted with a temporal frequency slightly lower than the neuron's optimum for LM gratings (Mareschal and Baker 1999). A high spatial frequency sinusoidal grating was used as a carrier, with a contrast of 70%. This carrier grating was held stationary except for measurements of carrier temporal frequency selectivity, in which it was drifted with varying temporal frequency. Motion-defined boundaries were generated using "velocity modulation" (VM) gratings, in which alternate half-cycles of the envelope contained a texture (carrier) moving with different velocities. This envelope was parallel to the motion direction of the carrier (shear), and it drifted in a direction perpendicular to the carrier motion with the same temporal frequency (between 1 and 4 Hz) used for CM gratings. In particular, we tested two types of velocity modulation gratings: unidirectional (Fig. 1*C*) and bidirectional (Fig. 1*D*). In unidirectional VM gratings, alternate half-cycles of the envelope contained a moving or stationary carrier. Bidirectional boundaries were created by oppositely moving carriers. For CM gratings, the envelope was sinusoidal, whereas for VM gratings it was a square wave. All stimuli were presented within a

raised cosine-tapered circular window against a gray background of the same mean luminance. On some trials, a uniform gray screen was presented to measure spontaneous activity.

Extracellular recording. Spikes from single neurons were recorded extracellularly with glass-coated platinum/iridium and parylene-coated tungsten single-channel microelectrodes (Frederick Haer) and 16 channel multielectrodes (Neuronexus). Spike times were collected through a lab interface (ITC-18, Instrutech) at 100-μs resolution, and, simultaneously, the raw data signals were also acquired with a Plexon recorder (filtered at 3 Hz to 8 kHz, sampled at 40 kHz) and streamed to hard disk for later analysis. Single units were isolated using a window discriminator (Frederick Haer) and displayed on a delay-triggered digital oscilloscope. When recordings with multielectrodes were made, spikes from one selected channel were analyzed online and used to guide the recording protocol (below). A photocell (TAOS, TSL12S) was used for the temporal registration of stimulus onset/offset timing and spike recordings.

A manually controlled bar-shaped stimulus was used to search for neural signals and to determine location of the receptive field, ocular dominance, eccentricity, and approximate optimal orientation. The CRT monitor was centered on the neuron's receptive field, and the nondominant eye was occluded. Drifting sine-wave luminance gratings were used to measure the neuron's luminance passband (spatial frequency, orientation, and temporal frequency tuning), with each stimulus condition randomly interleaved and repeatedly presented for 10–20 times. The neuron's optimal LM grating was then presented in small circular patches in different locations on the screen to more accurately map the receptive field, and the screen was recentered if necessary. To measure the size of the receptive field and check for surround suppression, the optimal LM grating was presented in circular patches of varying sizes centered on the receptive field.

As an initial assessment of responsiveness to second-order stimuli, responses to drifting CM gratings were recorded with a stationary carrier, an envelope orientation at the neuron's optimal luminance orientation, an envelope spatial frequency equal to or lower than the neuron's optimal luminance spatial frequency, and an envelope temporal frequency slightly lower than the neuron's optimal luminance temporal frequency (Zhou and Baker 1996; Mareschal and Baker 1999). A series of carrier spatial frequencies were tested, ranging from values near the screen resolution to the neuron's luminance passband, to find the optimal carrier spatial frequency. We classified a neuron as second-order responsive if it gave significant responses compared with spontaneous activity (*t*-test) at relatively high carrier spatial frequencies that were well outside the luminance passband of the neuron and if this spatial frequency tuning was band pass. This condition of band-pass tuning ensured that the neuron's response was genuinely second order and not due to a nonlinearity in the screen, which might give rise to a luminance signal at the envelope spatial frequency (Zhou and Baker 1994). If the neuron was classified as second-order responsive, then responses to VM gratings were recorded by testing a series of carrier spatial frequencies, with envelope orientation fixed to the neuron's optimal luminance orientation. If a neuron responded significantly to VM gratings, then envelope orientation tuning was measured using the neuron's optimal carrier spatial frequency, with carrier orientation always kept perpendicular to the envelope orientation. The temporal frequency of the drifting carriers in VM gratings was then varied to study carrier temporal tuning properties. The temporal frequency response for the carrier of CM gratings was also obtained for comparison with the VM results.

Analysis. Neurons were classified as either simple or complex type by measuring the ratio of modulated (first harmonic) to mean responses [$F_1/(F_0$ − spontaneous), or "alternating current-to-direct current ratio"] to the neuron's optimal LM grating. If the ratio was >1, the neuron was classified as a simple type cell; otherwise, it was classified as a complex cell (Skottun et al. 1991). Neuronal responses used in the formulas below had spontaneous activity subtracted from them.

Spatial frequency tuning curves were fit with a Gaussian function (DeAngelis et al. 1994) to obtain an estimated optimal spatial frequency, as follows:

$$R(sf) = ke^{-(sf - SF_{opt}/\alpha)^2} + R_o \qquad (1)$$

where R(sf) is the neuronal response at spatial frequency sf, and k, SF_{opt}, α, and R_o are free parameters. A bootstrap resampling method (Efron and Tibshirani 1993) was used to estimate 95% confidence intervals for the obtained optimal spatial frequency (R_{opt}) value.

For orientation tuning curves, circular variance (CV) was calculated as an index of tuning bandwidth (Marida 1972) as follows:

$$CV = 1 - \frac{\left| \sum_k R_k \exp(i2\theta_k) \right|}{\sum_k R_k} \qquad (2)$$

where R_k represents the neuronal response at orientation θ_k. CV ranged from zero (sharp tuning) to unity (isotropic tuning). Optimal orientation (Ori_{opt}) was estimated as follows:

$$Ori_{opt} = \arg\left[\frac{\sum_k R_k \exp(i2\theta_k)}{\sum_k R_k} \right] \qquad (3)$$

where arg is the angular component of a complex number.

Motion direction selectivity of a neuron was measured by a direction selectivity index (DSI), as follows:

$$DSI = (R_P - R_N)/(R_P + R_N) \times 100\% \qquad (4)$$

where R_P is the response of the neuron to its preferred direction of motion and R_N is the response to its nonpreferred direction. DSI ranged from 0% (nondirectional) to 100% (completely directional).

Neurons' responses to a series of carrier temporal frequencies in both directions of motion were tested for CM and unidirectional VM gratings. The extent to which these data revealed direction selectivity to carrier motion was summarized by a symmetry index (SI), as follows:

$$SI = 1 - \frac{\sum_k \left| R_k - R_{-k} \right|}{\sum_k \left| R_k + R_{-k} \right|} \qquad (5)$$

where R_k is the response of the neuron to VM or CM gratings with carrier drifting at k Hz and R_{-k} is the response to stimuli with carrier drifting at k Hz in the opposite direction. SI would be 0 if the neuron responds only to one direction of carrier motion and not to the other (direction selective), and it would be 1 if the neuron responds equally to both directions of carrier motion (nondirection selective).

The proportional decline in response of a neuron at high temporal frequency compared with its optimal response was given by the following falloff index (FI):

$$FI = (R_H)/(R_{max}) \qquad (6)$$

where R_H is the response of a neuron at high temporal frequency and R_{max} is the maximal (optimal) response. FI was calculated for responses of a neuron to LM gratings as well as VM and CM gratings. In the case of LM gratings, R_H is the response to gratings drifting at 16 Hz and R_{max} is the response at the optimal temporal frequency. In the case of VM and CM gratings, R_H is the response to VM or CM gratings with carrier drifting at 16 Hz and R_{max} is the response to the same grating at its optimal carrier temporal frequency. FI ranged from 0 (response fell to spontaneous at 16 Hz) to 1 (optimal response at 16 Hz over the measured range of 0–16 Hz).

To evaluate whether a neuron exhibited a similar preference for the two kinds of gratings, Pearson's correlation coefficient was calculated for scatterplots comparing optimal carrier spatial frequencies for CM and VM gratings and optimal orientations for LM gratings and the

envelope of VM gratings. In addition, nonparametric, paired comparisons (Wilcoxon signed-rank test) were performed.

For recordings with multielectrodes, spikes from only one channel were analyzed online to construct tuning curves. In the later offline analysis, spikes from other channels were detected and classified using Offline Sorter software (version 2.8.8, Plexon). Spikes were sorted using the "semiautomatic *K*-means" algorithm, and only clearly separable clusters of spikes were classified as single units. Isolated neurons from these channels were included in further analysis only if they showed very similar tuning to orientation and spatial frequency of LM gratings compared with the neuron recorded online. In some cases for recordings with single-channel electrodes, offline sorting of spikes was performed to correct misclassifications by the window discriminator and to isolate and assess spikes with lower amplitude.

Model. To explore to what extent the model scheme shown in Fig. 1, *E* and *F*, could provide an understanding of the general features of these neuronal responses, we constructed a computer simulation in Matlab. The architecture of the model (Fig. 1*E*) consisted of two parallel processing pathways, a linear filter F_0 responding to luminance (first order) stimuli and a nonlinear pathway (F1-R-F2; Fig. 1*F*) processing nonluminance (second order) stimuli.

Filter F_0 is a spatiotemporal filter constructed by taking a dot product of each frame of the stimulus with a gabor spatial filter to produce a temporal signal that is then convolved with the temporal filter (Adelson and Bergen 1985). Finally, this signal is half-wave rectified to give a simple cell-like modulated response.

$$\text{tfilt}(t) = \frac{(k \times t)^n e^{-k \times t}}{n!} - \frac{(k \times t)^2}{n+2} \qquad (7)$$

where tfilt is the temporal filter, *t* is time, *k* is a constant, and $n = 2$. *k* was calculated using the following equation:

$$k = \text{tm}_{scl}^2 \times \text{tf}_{opt}/1,000 \qquad (8)$$

where tm_{scl} is a timescale factor defined as milliseconds/frame and tf_{opt} is the optimal temporal frequency of the filter.

The first stage of the nonlinear pathway contained a pool of spatiotemporal filters (F_1), which was implemented by convolving each spatial frame stimulus with a gabor spatial filter followed by temporal convolution with a monophasic temporal filter (Watson and Ahumada 1985), as follows:

$$\text{tfilt}(t) = (k \times t)^n e^{-k \times t} \qquad (9)$$

where $n = 0$ and *k* is given by *Eq. 8*, where tf_{opt} was set to 1 Hz.

Each of these temporal responses was then full-wave rectified and summed by a spatiotemporal filter (F_2), which was constructed exactly the same as filter F_0. The action of filter F_2 on the rectified signals was also implemented as a dot product in the same manner as in the linear pathway, and the output of filter F_2 was then half-wave rectified to give a simple cell-like modulated response.

Finally, the temporal output signals of these two pathways were summed to give the final output of the model. Note that the output of this model is an analog signal representing average spike frequency as a function of time rather than discrete spiking events.

We did not try to fit parameters of these filters to the data from individual neurons but instead used a generic model with fixed values of parameters, because our aim here was to explore to what extent the nonlinear FRF model that has been proposed to process second-order stimuli (Baker and Mareschal 2001) can provide some understanding of these data. Model responses were measured to the same stimuli used in the experimental recordings of the neuronal responses. The parameters of the model were as follows: for filter F_0, the spatial frequency of the gabor was 0.08 cycles/° (cpd), the spatial bandwidth was 1.5 octaves, the aspect ratio (defined as the ratio of the filter's axial length to cross-width) was 1, the orientation was 0°, and the optimal temporal frequency was 2 Hz. For filter F_1, the spatial frequency of the gabor was 1.6 cpd, the spatial bandwidth was 1.5

octaves, the aspect ratio was 1, the orientation was 90°, and the parameters of the monophasic temporal filter were $n = 0$ and $\text{tf}_{opt} = 1$ Hz, which were chosen to provide selectivity to the carrier temporal frequency of CM gratings roughly like those shown by neurons (see Fig. 8, *C–H*). The parameters for filter F_2 were identical to those for filter F_0.

RESULTS

For this study, we recorded from 115 area 18 neurons in 13 cats. Of these, 64 neurons (55%) were classified as second-order-responsive neurons, as they responded significantly to CM gratings and showed band-pass tuning to its carrier spatial frequency. These second-order-responsive neurons were further tested with VM gratings (motion defined) of two types: unidirectional and bidirectional. Carrier spatial frequency and envelope orientation tuning were also measured using unidirectional VM gratings, which gave stronger responses than bidirectional VM gratings.

Carrier spatial frequency selectivity. Previous studies have demonstrated that second-order-responsive neurons in area 18 show narrow band-pass tuning to carrier spatial frequency of CM gratings well outside their luminance passband (e.g., Zhou
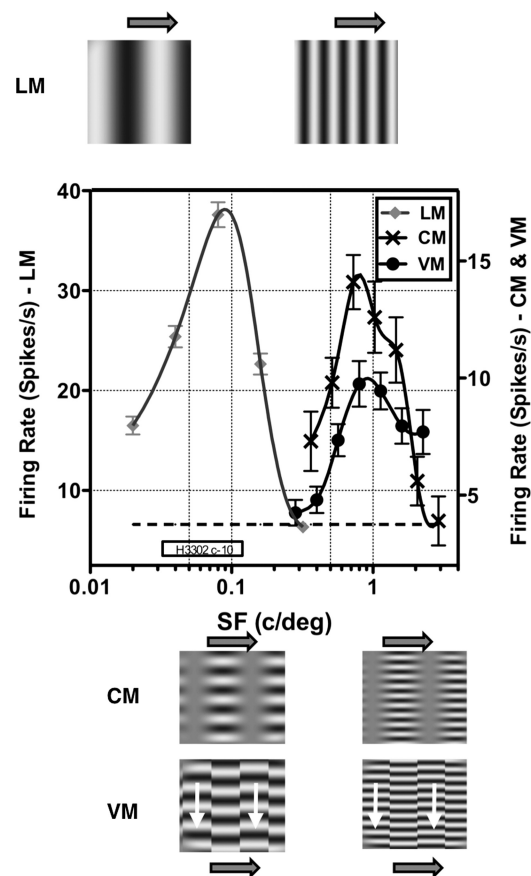

Fig. 2. Responses of a typical neuron to LM, CM, and VM gratings. Neuronal responses to LM gratings are shown as a function of SF measured at the grating's optimal orientation. Snapshots of luminance gratings with two different SFs are shown at the *top*. Optimal luminance SF for this neuron was 0.08 cpd, and the neuronal response fell to spontaneous activity (dashed line) at 0.3 cpd. Responses of the same neuron were measured to CM and VM gratings as a function of carrier SF. Carrier SF tuning for both gratings was very similar, with peaks around 0.8 cpd, much greater than the optimal luminance grating SF of 0.08 cpd. Snapshots of CM and VM gratings with two different carrier SFs are shown at the *bottom*. cpd, cycles per degree.
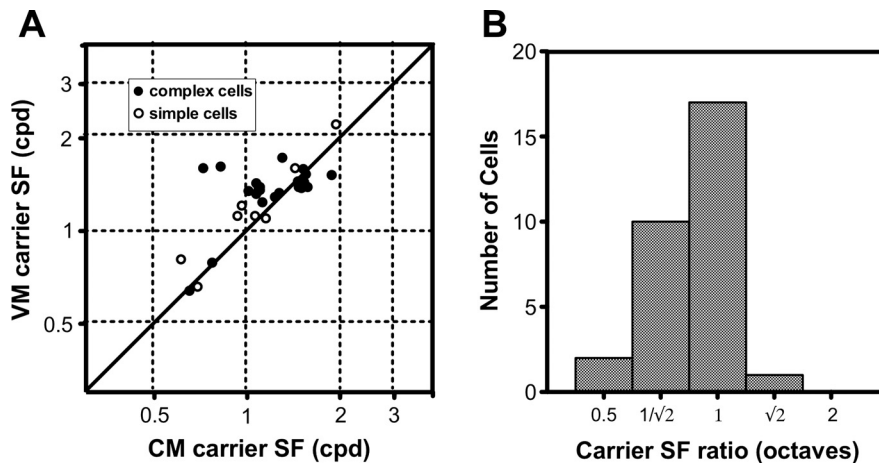
Fig. 3. Relationship between optimal carrier SF for VM and CM stimuli. *A*: scatterplot showing neurons' optimal carrier SF for VM gratings versus CM gratings for 30 neurons (21 complex cells and 9 simple cells). A given neuron's optimal carrier SF for VM gratings was highly correlated with that for CM gratings ($r = 0.7$, $P < 0.0001$). *B*: histogram showing ratios of optimal carrier SFs for CM and VM gratings in octaves.

and Baker 1996; Mareschal and Baker 1998; Tanaka and Ohzawa 2006; Rosenberg and Issa 2011). Thus, we wanted to see if these neurons would also show similar selectivity to carrier spatial frequency of VM gratings. The neuron shown in Fig. 2 showed band-pass tuning to luminance gratings (0.02–0.2 cpd, with a peak response at 0.08 cpd). The CM gratings were tested with varying carrier spatial frequencies, with envelope orientation fixed at the neuron's optimal luminance orientation. This neuron showed band-pass tuning to carrier spatial frequency with a response peak at ~0.8 cpd. At this high spatial frequency range, the carrier signals were well beyond the neuron's luminance resolution, and, hence, it was classified as a second-order-responsive neuron. This neuron was further tested with VM gratings for varying carrier spatial frequencies, with envelope orientation fixed at the neuron's optimal luminance orientation. This neuron showed similar band-pass tuning to carrier spatial frequency as shown for CM gratings, again with a response peak at ~0.8 cpd. In this plot, the neuron's responses are shown on different scales for carrier spatial frequency tuning and LM spatial frequency tuning, since this neuron's LM grating response was much stronger than those to the CM and VM gratings.

The scatterplot shown in Fig. 3*A* shows a given neuron's optimal carrier spatial frequency for VM gratings against that

for CM gratings for 30 neurons (9 simple neurons and 21 complex neurons). Points on the scatterplot were highly correlated [$r = 0.7$, $P < 0.0001$, 95% confidence intervals (CIs; 0.46–0.85)], and most of the points on the scatterplot were close to the equality line, indicating that carrier spatial frequency tuning was similar for both types of gratings. Only 1 neuron of the 30 total had significantly different optimal carrier spatial frequencies for 2 stimuli (bootstrap method, CI = 95%). Figure 3*B* shows a histogram plotted for ratios of optimal carrier spatial frequencies between CM and VM gratings, which was centered on one.

Envelope orientation selectivity. To assess form-cue invariance for luminance- and motion-defined boundaries, like that previously demonstrated for luminance- and contrast-defined boundaries (Mareschal and Baker 1998a), we measured the orientation selectivity of neurons to the envelope of unidirectional VM gratings for a comparison with that of LM gratings. Figure 4*A* shows responses of a typical neuron that was tuned to the orientation as well as motion direction of luminance gratings (Ori$_{opt}$: 97° and DSI: 0.94). This neuron also showed similar orientation tuning for the envelope of VM gratings (Ori$_{opt}$: 91°; Fig. 4*B*) and was also direction selective, although to a somewhat smaller degree (DSI: 0.55). We also measured envelope orientation tuning for CM gratings for this neuron
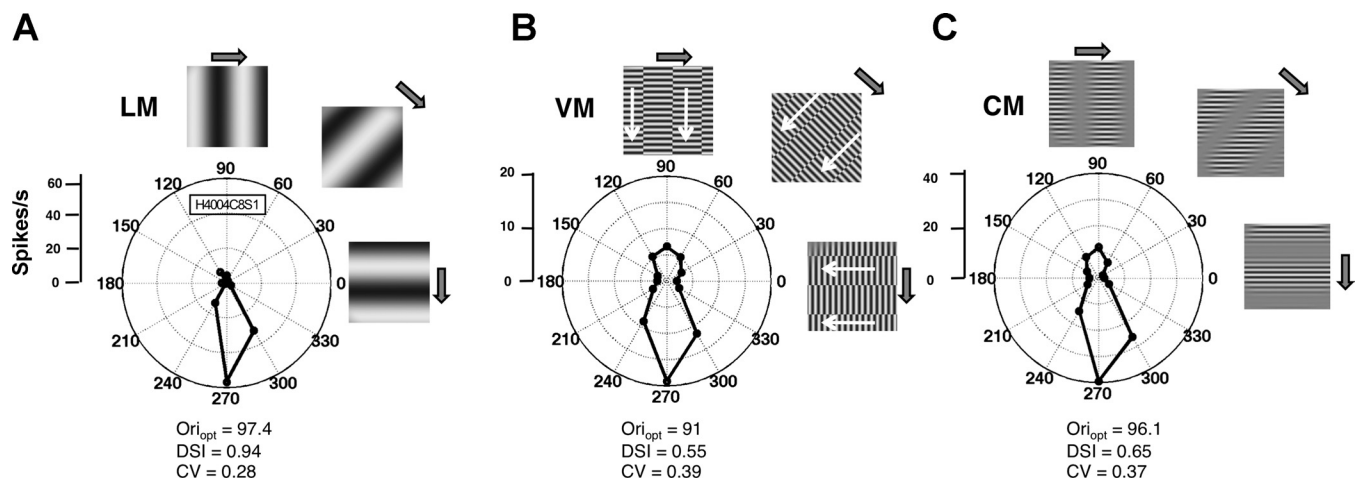

Fig. 4. Orientation tuning of a typical neuron to LM gratings and envelopes of VM and CM gratings. In these polar plots, distance from the origin indicates the neural response (in spikes/s); the angular subtense represents envelope orientation (0–360°). Snapshots of LM, VM, and CM gratings at three different orientations are shown next to the polar plots. Optimal orientation (Ori$_{opt}$), direction selectivity index (DSI), and circular variance (CV) are shown at the *bottom* of each polar plot. This neuron showed similar orientation tuning and direction selectivity for all three stimuli, i.e., form-cue invariance.

(Ori$_{opt}$: 96.1° and DSI: 0.37; Fig. 4*C*), which showed tuning very similar to that for VM gratings.

The scatterplot shown in Fig. 5*A* shows a given neuron's optimal envelope orientation for VM gratings against the optimal orientation for LM gratings for 26 neurons (10 simple neurons and 16 complex neurons). Points on the scatterplot were highly correlated [$r = 0.95$, $P < 0.0001$, 95% CI (0.89–0.98)], and most of the points were close to the equality line. Fifteen of twenty-six neurons (58%) had optimal orientation differences of <15°, with a maximum orientation difference of 37°. There was no significant difference between a given neuron's optimal orientation for LM gratings and optimal envelope orientation for VM gratings ($P = 0.34$ by Wilcoxon signed-rank test). The histogram shown in Fig. 5*B* shows that differences in optimal orientations were very small (mean: −4.4°). The scatterplot shown in Fig. 5*C* shows a given neuron's envelope orientation CV for VM gratings against the orientation CV for LM gratings. Most of the points (23 of 26) were above the equality line, indicating broader tuning for VM compared with LM gratings. The CV for VM gratings was significantly greater than for LM gratings ($P < 0.0001$ by Wilcoxon signed-rank one-tailed test). The scatterplot

shown in Fig. 5*D* shows a given neuron's DSI for the motion direction of the envelope of VM gratings versus the motion direction of LM gratings. Most of the points (18 of 26) were in the first quadrant, suggesting that most neurons preferred the same direction of motion for both kinds of stimuli. The DSI for LM gratings (mean: 0.52) was significantly greater than for VM gratings (mean: 0.23, $P = 0.0008$ by Wilcoxon signed-rank one-tailed test), suggesting that neurons had weaker direction selectivity for VM compared with LM gratings.

Note that if a neuron was responding to the carrier motion, then the optimal envelope orientation for VM gratings would be orthogonal to that of LM gratings (since the carrier was always orthogonal to the envelope in these experiments), and the histogram shown in Fig. 5*B* would peak around 90° instead of 0°. However, this was not the case; instead, these results demonstrate that neurons' VM grating responses are to the envelope and not to the local motion of the carrier and that they occur in a form-cue invariant manner.

Carrier temporal frequency tuning. A previous study (Mareschal and Baker 1998b) demonstrated that most of the second-order-responsive neurons in cat area 18 showed band-pass tuning to the temporal frequency of drifting envelopes of CM gratings. Neurons were systematically selective for lower envelope temporal frequencies of CM gratings compared with LM gratings. Responses of these neurons usually fall off to spontaneous activity above an envelope temporal frequency of ~10 Hz, whereas for luminance gratings, responses fall off around 16 Hz. To see if neurons show similar tuning properties to drifting carriers, we measured responses for CM and both unidirectional and bidirectional VM gratings for varying carrier temporal frequencies. Note that the envelopes of CM and both unidirectional and bidirectional VM gratings were drifted at a fixed temporal frequency that was slightly lower than the neuron's optimal temporal frequency for LM gratings.

For unidirectional VM gratings, one carrier was always held stationary and the other drifted at varying temporal frequencies in both directions. For some neurons, the response decreased with increasing temporal frequency (Fig. 6*C*); the response of some neurons increased with temporal frequency (Fig. 6*E*), some neurons responded equally to all temporal frequencies (Fig. 6*F*), a few neurons showed band-pass tuning (Fig. 6*D*), and some neurons showed no such particular pattern (Fig. 6, *G* and *H*). Interestingly, almost all neurons showed symmetric tuning, i.e., a similar response pattern for both directions of carrier motion, indicated by SI values close to 1 in Fig. 6. The scatterplot shown in Fig. 9*A* shows a given neuron's FI for unidirectional VM gratings against that for LM gratings. Most of the points (19 of 24) were above the equality line, suggesting that for unidirectional VM gratings, neuronal responses fall off at high temporal frequencies relatively less than for LM responses. FI values were significantly greater for VM gratings compared with LM gratings ($P = 0.0018$ by Wilcoxon signed-rank one-tailed test).

For bidirectional VM gratings, the carrier gratings drifted with equal and opposite velocities. Figure 7 shows carrier temporal frequency tuning for six neurons. The responses for most neurons in our sample decreased with increasing temporal frequency (e.g., Fig. 7, *C–G*), except for one (Fig. 7*H*), which showed band-pass tuning. This was the only neuron that
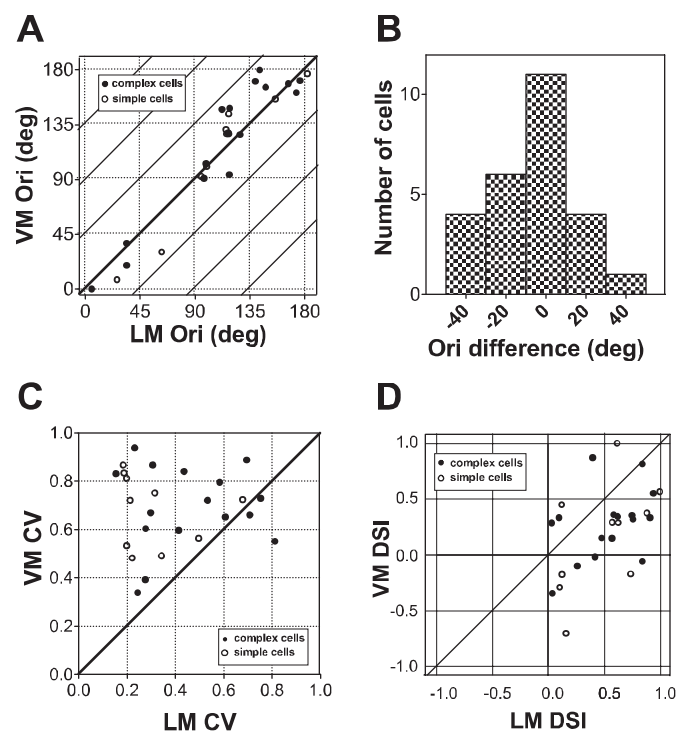

Fig. 5. Relationship between orientation (Ori) and direction selectivity for VM and LM stimuli for a sample population of neurons. *A*: scatterplot showing neurons' optimal envelope orientation for VM gratings versus optimal orientation for LM gratings for 26 neurons (10 simple cells and 16 complex cells). A given neuron's optimal envelope orientation for VM gratings was highly correlated with its optimal orientation for LM gratings ($r = 0.95$, $P < 0.0001$). *B*: histogram showing differences between optimal orientations for VM and LM gratings. *C*: scatterplot showing a given neuron's envelope orientation CV for VM gratings versus orientation CV for LM gratings. Most of the points (23 of 26) were above the equality line, indicating broader tuning for VM gratings compared with LM gratings. *D*: scatterplot showing a given neuron's DSI for the motion direction of the envelope of VM gratings versus the motion direction of LM gratings. Most neurons (18 of 26) preferred the same direction of motion for LM and VM gratings. The remaining neurons, which preferred opposite directions, were weakly direction selective to at least one of the two gratings.
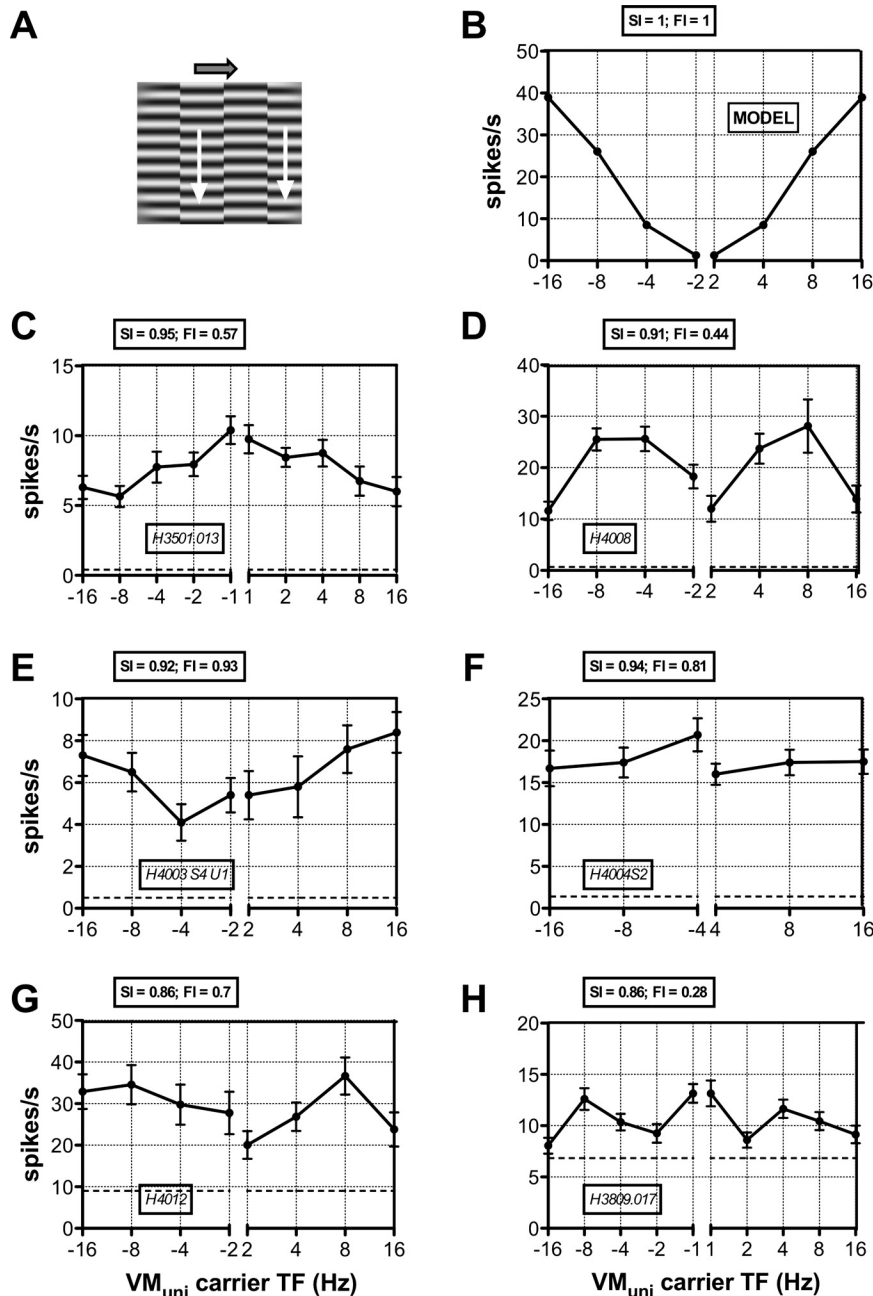
Fig. 6. Carrier TF responses to unidirectional VM gratings (VM$_{uni}$; A), for the model (B), and for six neurons (C–H). Different neurons showed diverse tuning properties to carrier TF, but most responded significantly to a broad range of TFs tested, with similar tuning for both directions of carrier motion. Responses of the model (whose parameters were chosen based on CM responses; see Fig 8) increased with carrier TF. Negative values of carrier TF signify carrier motion in the opposite direction. Dashed lines indicate spontaneous activity. Symmetry index (SI) values represent symmetry of responses to both directions of carrier motion, and falloff index (FI) values represent the relative fall in response at carrier TF of 16 Hz compared with the maximum response.

showed band-pass tuning in our sample of 19 neurons; all others gave low-pass responses.

In most previous single-unit studies using CM stimuli, the carrier grating was always held stationary while the envelope was drifting (Zhou and Baker 1993, 1994; Mareschal and Baker 1998a, 1999; Song and Baker 2007; Rosenberg and Issa 2010). In our present study, to measure the dynamic properties of early stages of a FRF model, we measured temporal frequency tuning for drifting carriers of CM gratings, similar to a recent study (Rosenberg and Issa 2011). Since we wanted to compare this CM carrier temporal frequency tuning with the carrier tuning for VM gratings, we maintained the carrier orientation perpendicular to the envelope orientation for CM gratings and varied carrier temporal frequency from 0 to 16 Hz (with 0 Hz corresponding to a stationary carrier). Figure 8 shows carrier temporal frequency tuning for six neurons.

Consistent with Rosenberg and Issa (2011), our sample neurons showed very diverse tuning, but most of them responded optimally to a stationary carrier, and the response decreased with increases in temporal frequency. Since the carrier of the CM gratings was stationary while we evaluated the neurons' second-order responsivity, we might have inadvertently excluded in our sample any neurons that preferentially respond to CM gratings with drifting carriers (Rosenberg and Issa 2011). However, some neurons also responded quite well to very high temporal frequencies (Fig. 8, F and H). Similar to the results from unidirectional VM gratings, neurons usually showed symmetric tuning to carrier temporal frequency, i.e., the response pattern was similar to both directions of carrier motion (indicated by SI values close to 1 in Fig. 8). The scatterplot shown in Fig. 9B shows a given neuron's FI for CM gratings against that for
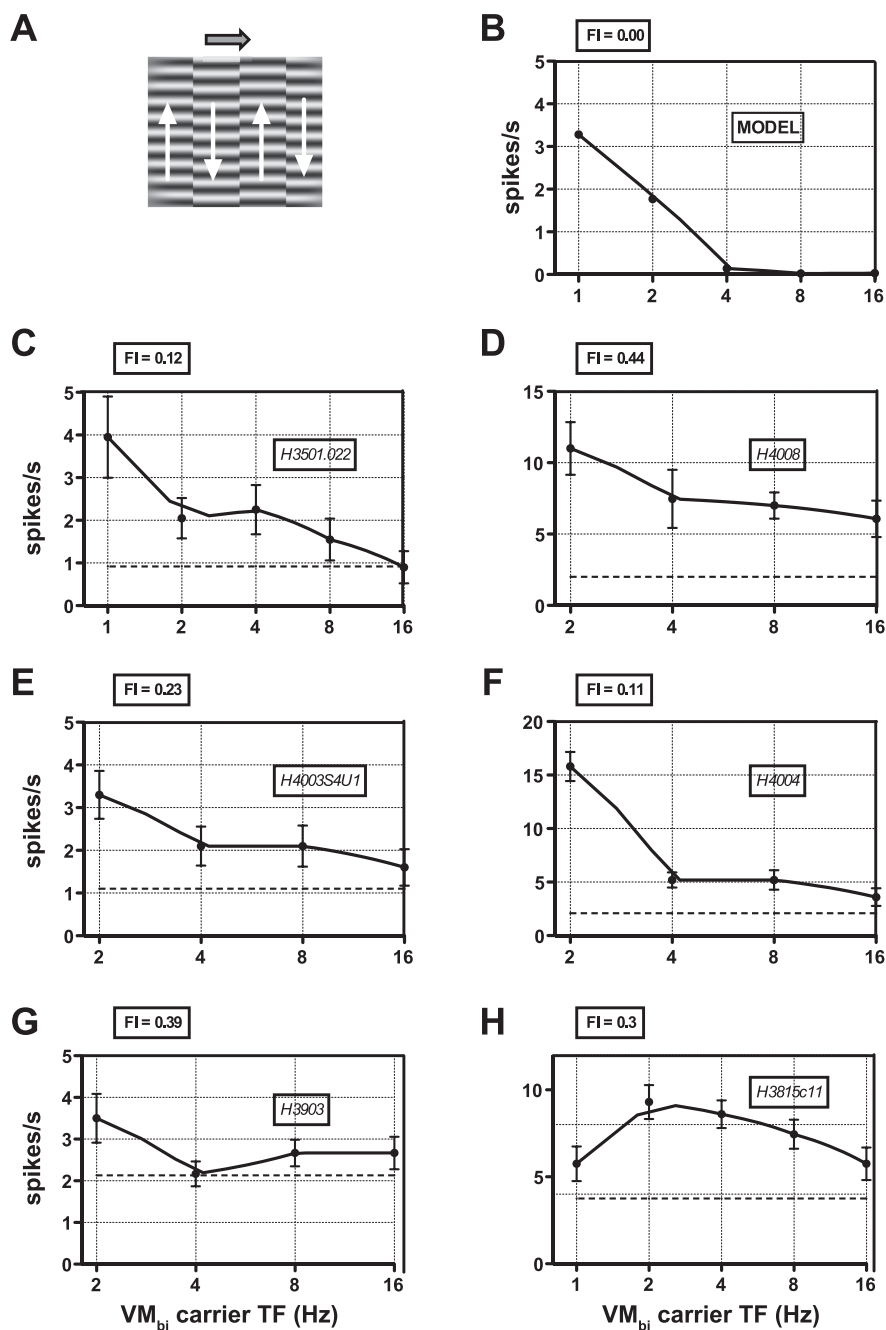
Fig. 7. Carrier TF responses to bidirectional VM gratings (VM$_{bi}$; *A*), for the model (*B*), and for six neurons (*C–H*). Responses of the model (*B*) decreased with increasing carrier TF. Similar to the model, responses of the neurons typically decreased with increasing carrier TF (*C–G*), whereas one neuron (*H*) showed band-pass tuning. Dashed lines indicate spontaneous activity. FI values are shown at the *top* of each plot.

LM gratings. There was no systematic relationship between FIs for these two gratings, and FI values were not significantly different for CM and LM gratings ($P = 0.98$ by Wilcoxon signed-rank two-tailed test).

Responsiveness to unidirectional and bidirectional gratings. To assess how well CM-responsive neurons also responded to both uni- and bidirectional VM gratings, we compared response strengths for the two stimuli at their optimal carrier temporal frequencies. The scatterplot shown in Fig. 10*A* shows the response strength to bidirectional versus unidirectional VM gratings for 19 neurons (5 simple neurons and 14 complex neurons) from carrier temporal frequency data like those shown in Figs. 6 and 7. All the data points were on or below the equality line, indicating that neurons responded more strongly to unidirectional VM gratings; this difference was

significant ($P < 0.0001$ by Wilcoxon signed rank one-tailed test). Even though all (19/19) of the second-order-responsive neurons responded significantly to unidirectional VM gratings, some neurons (9/19) failed to respond significantly (one-tailed *t*-test) to bidirectional gratings. The histogram (Fig. 10*B*) showing the ratio of response strength to uni- and bidirectional stimuli demonstrates that for all neurons, the ratio was less than or equal to unity and that for 16 of 19 neurons, the ratio was <0.6. The scatterplot and histogram show results only for those second-order-responsive neurons that were tested with both types of VM gratings.

Envelope spatial frequency tuning. Conceivably, VM gratings might be detected in two different ways: dynamic discontinuities between moving carriers ("edge-based" processing) or by relative speeds of the carriers ("region-based" processing)
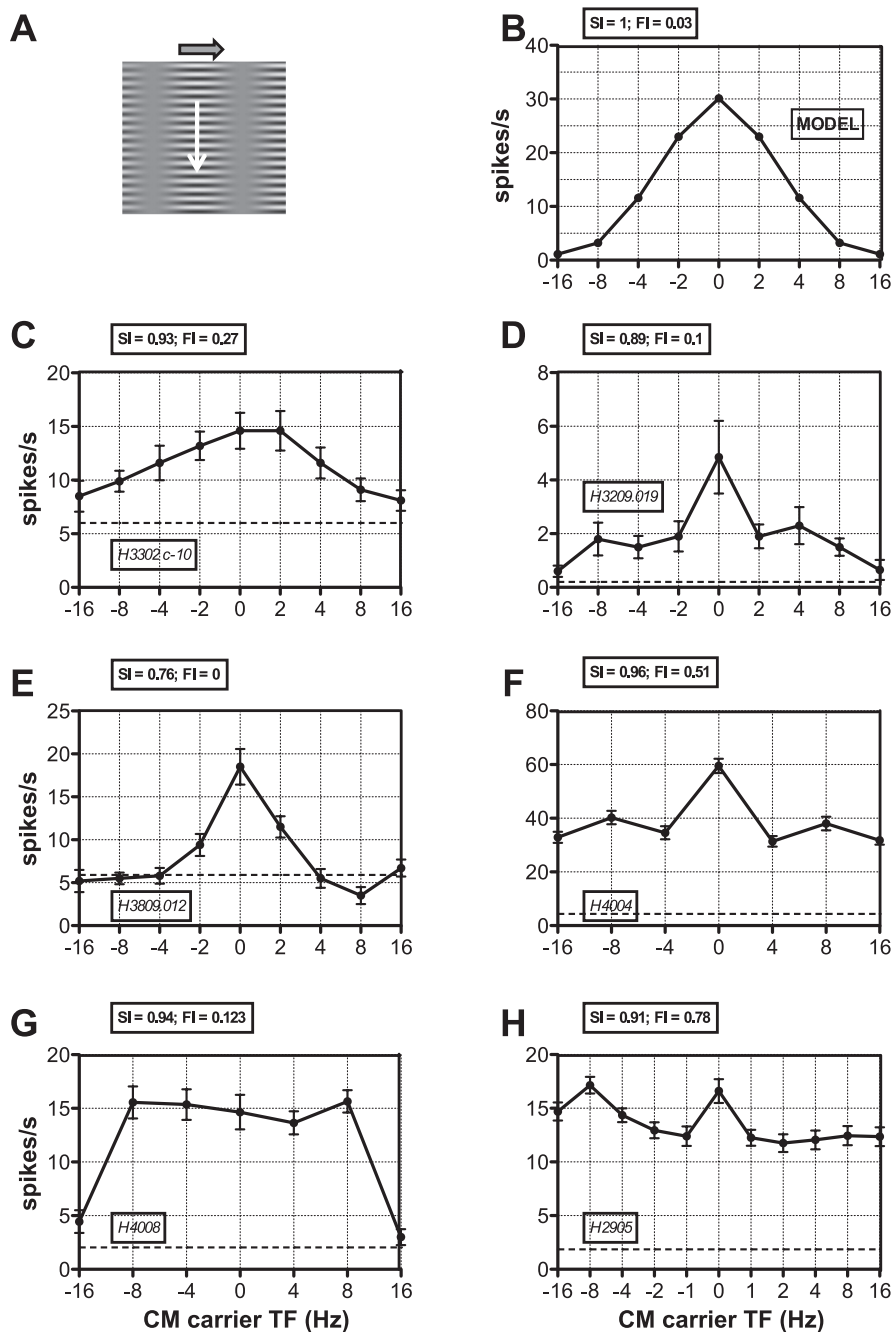
Fig. 8. Carrier TF responses to CM gratings (*A*), for the model (*B*), and for six neurons (*C–H*). The orientation of the carrier grating was kept perpendicular to the envelope orientation, and TF was varied from 0 Hz (stationary carrier) to 16 Hz in both directions. The model responded optimally to a stationary carrier, and the response decreased with increasing carrier TFs. Neurons responded similarly to the model (*C–F*), although some neurons responded equally well to drifting carriers (*G* and *H*). Neurons showed similar tuning for both directions of carrier motion. Negative values of carrier TF indicate motion in the opposite direction. Dashed lines indicate spontaneous activity. SI and FI values are shown at the *top* of each plot.

(see DISCUSSION). We measured envelope spatial frequency tuning curves to uni- and bidirectional VM gratings and compared them with the tuning for ICs, which are thought to be detected by edge-based processing (Song and Baker 2007). Interestingly, neurons were tuned to higher envelope spatial frequencies of unidirectional VM gratings compared with bidirectional ones. Neurons showed similar envelope spatial frequency selectivity for ICs and bidirectional VM gratings (Fig. 11*B*). This similarity suggests that bidirectional boundaries are detected in a manner like ICs, i.e., by dynamic phase discontinuities of the carrier textures along the boundary. However, neurons were selective for higher envelope spatial frequencies of unidirectional VM gratings compared with ICs, approximately two times the peak envelope spatial frequency for ICs (Fig. 11*A*). Therefore, unidirectional boundaries may

be detected primarily by differences in the speeds of textures between envelope half-cycles, i.e., region-based processing, with some additional contribution from dynamic discontinuities, i.e., edge-based processing.

Model simulation. We simulated an FRF model that has been previously proposed to explain the responses of area 18 neurons to CM gratings and ICs (Song and Baker 2007) to see how well it might also account for the responses of these neurons to VM gratings. The model parameters were not fit to a particular neuron's data, but rather a generalized model was constructed to simulate the typical selectivity patterns of area 18 neurons for CM gratings, which was then tested to see how well it could predict selectivity patterns for VM gratings. Temporal parameters of the early filters were selected to mimic typical neurons' responses to carrier temporal frequency of CM

A   **B**

Fig. 9. Comparison of FI values for unidirectional VM and CM gratings with LM gratings. *A*: scatterplot showing neurons' FI for unidirectional VM gratings versus LM gratings for 24 neurons. Most points were above the equality line (19/24), indicating that for VM gratings, neuronal responses fell off relatively less than LM responses at high TFs. *B*: scatterplot showing neurons' FI for CM gratings versus LM gratings for 22 neurons. There was no systematic relationship between FIs for these two gratings.
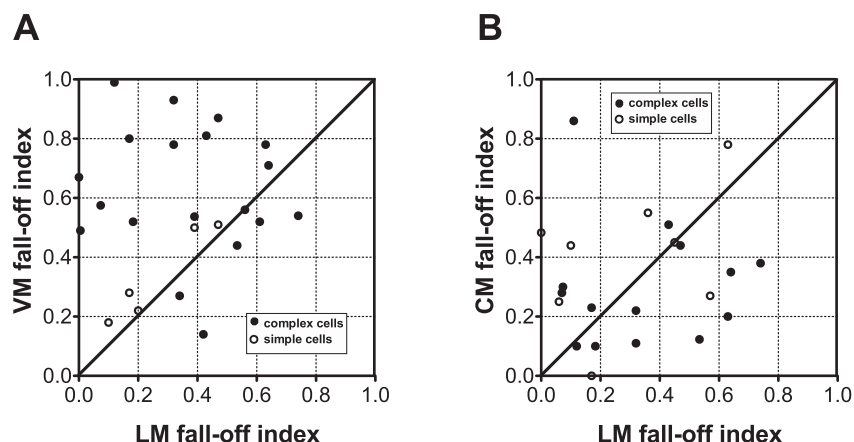
gratings, such that the model gave its best response to CM gratings with a stationary carrier and the response decreased with carrier temporal frequency (Fig. 8*B*), i.e., it gave a low-pass carrier temporal frequency response. These filters were not selective for the direction of carrier motion, in accordance with the neuronal responses (Fig. 8*B*) (Rosenberg and Issa 2011).

After the parameters of the model were fixed based on CM responses, we tested its selectivity to VM gratings and ICs. For unidirectional VM gratings, the response of the model increased with carrier temporal frequency (Fig. 6*B*). Although not all neurons' responses were exactly like this response pattern, most of the neurons' responses did remain significantly above spontaneous activity at high carrier temporal frequencies, as indicated by the FI shown in Fig. 9*A*. On the other hand, the model's response decreased with carrier temporal frequency for bidirectional VM gratings (Fig. 7*B*), similar to the response pattern of nearly all the neurons in our sample. And also similar to the neurons' responses, the model responded less strongly to bidirectional than to unidirectional VM gratings. Interestingly, the model showed similar envelope spatial frequency selectivity for ICs and bidirectional VM gratings (Fig. 11*B*), whereas it was selective for an envelope spatial frequency of unidirectional gratings that was twice that for ICs (Fig. 11*A*). These VM and IC envelope spatial frequency selectivity results were similar to those for neurons, thus supporting our hypothesis that bidirectional gratings are detected by edge-based processing, similar to ICs, whereas

unidirectional gratings are detected predominantly by region-based processing.

DISCUSSION

This study demonstrated that neurons in the early visual cortex can respond to motion-defined contours. These neurons were selective to similar orientations of luminance- and motion-defined contours as well as similar directions of motion (form-cue invariance), although the strength of direction selectivity was weaker for motion-defined contours compared with luminance-defined contours. These neurons were also selective for the spatial frequency of the carrier gratings used for constructing motion-defined contours. This carrier selectivity was very similar to the selectivity shown for the carrier of contrast-defined contours. These findings suggest that both kinds of contours are detected by the same nonlinear neural mechanism. Responses to both contrast- and motion-defined boundaries often extended to quite high temporal frequencies of drifting carrier gratings to which most cortical neurons fail to respond when tested with luminance gratings. However, for a given neuron, tuning was similar for both directions of carrier motion.

Sinusoidal grating carrier. It might seem counterintuitive to use sinusoidal gratings as a carrier instead of the random dot texture patterns used in previous studies (Chaudhuri and Albright 1997; Mysore et al. 2006; Sary et al. 1993, 1995; Zeki et al. 2003), as these patterns look more similar to texture

A   **B**

Fig. 10. Comparison of peak response amplitudes to unidirectional and bidirectional VM gratings. *A*: scatterplot showing a neurons' maximum response (in spikes/s) to bidirectional versus unidirectional VM gratings for 19 neurons. Neurons responded more strongly to unidirectional compared with bidirectional gratings. *B*: histogram showing the ratio of response strength of bidirectional gratings to unidirectional gratings. The ratio of the response strength was <0.6 for 16 of 19 neurons (84.2%).
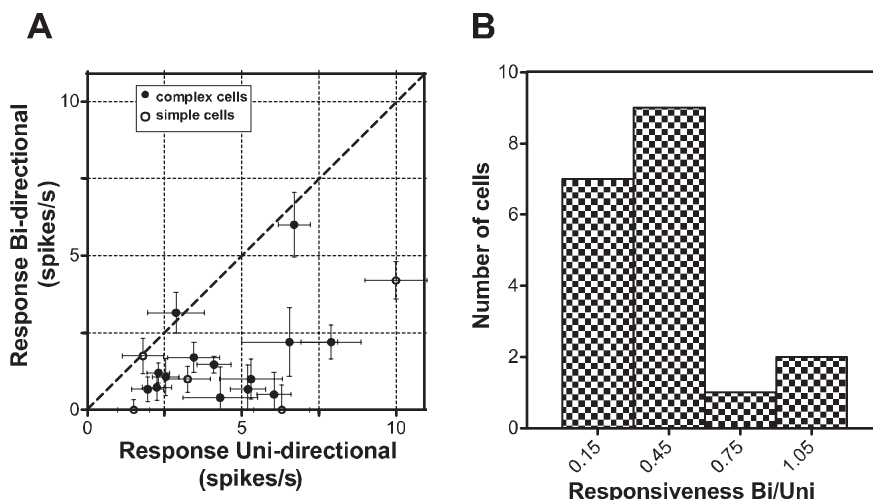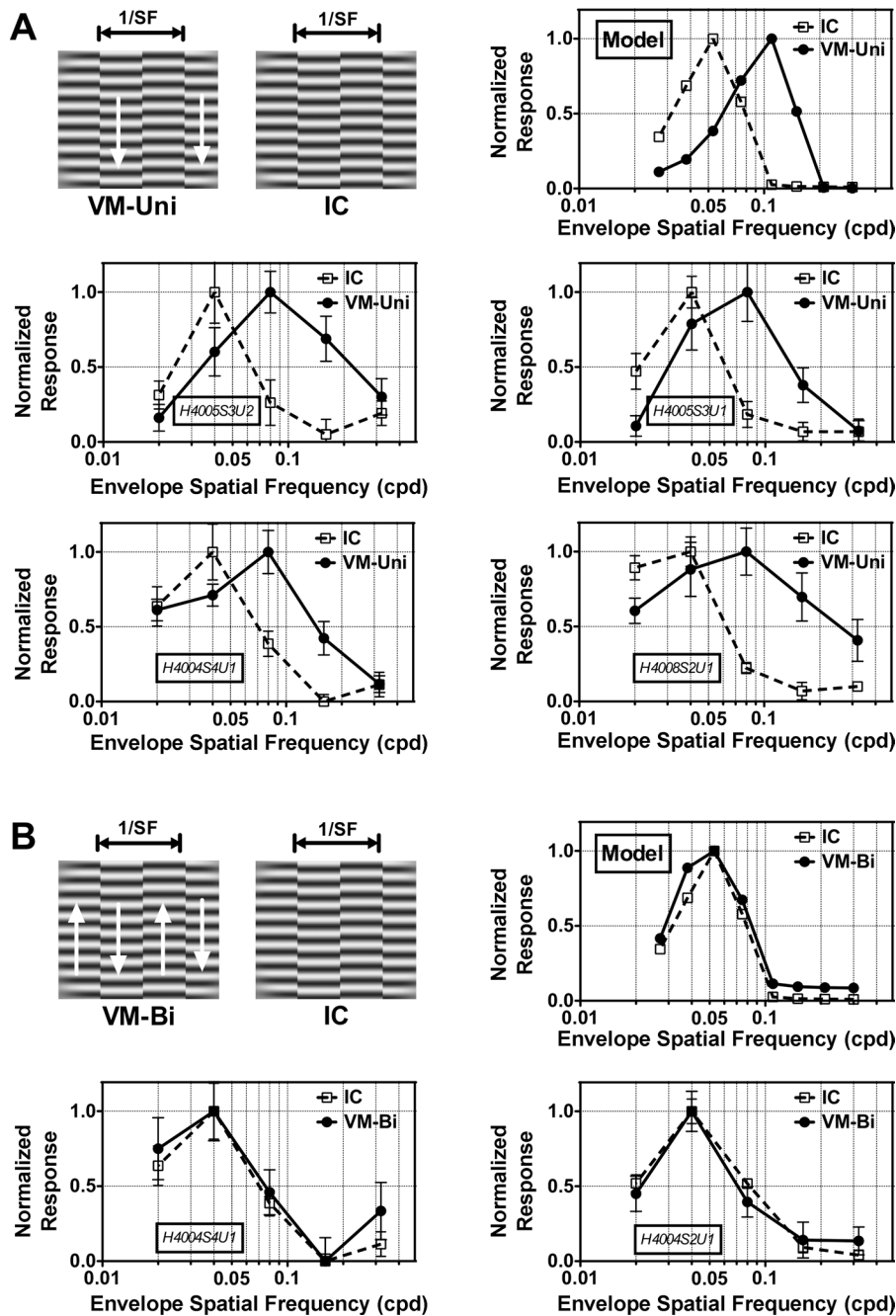
Fig. 11. Comparison of neurons' and model's envelope SF tuning to illusory contours (ICs) with that to VM gratings. *A*: comparison of responses to IC and unidirectional gratings. Responses from four neurons (*bottom* graphs) show that the preferred envelope SF for unidirectional VM gratings was two times higher than that for ICs, as predicted by the model (*top right* graph). *B*: comparison of responses to IC and bidirectional gratings. Responses from two neurons (*bottom* graphs) show that neurons' preferred envelope SFs for bidirectional VM gratings and ICs were the same, as also predicted by the model (*top right* panel).

patterns present in the real world. However, a sinusoidal grating carrier with spatial frequency outside a neuron's luminance passband provides powerful advantages in ruling out simple linear/luminance artifacts. First, it ensures that the responses are not mediated by the same linear filter thought to process luminance gratings. A random dot texture pattern, however, is broadband in spatial frequency, and some of its energy might fall within the luminance passband of a neuron, giving rise to a linear response. Second, these neurons show narrow carrier spatial frequency tuning, and this result rules out the possibility that their responses are mediated by early nonlinearities of the retina or CRT because such nonlinearities would not predict selectivity for carrier spatial frequencies.

However, VM stimuli with sinusoidal grating carriers introduce an ambiguity as to what the neuron is actually responding

to. If a snapshot image of VM stimuli is taken at some moment in time (Fig. 1*C*), then it looks like an illusory contour with phase discontinuities between two carriers. But, by measuring envelope spatial frequency tuning to VM gratings as described below, we were able to disambiguate between responses to phase discontinuities and difference in speeds of carriers. Note that in natural scenes, shear motion between textures will give rise to both of these cues: phase discontinuities and relative speed.

Neural mechanism. A model consisting of two parallel signal-processing streams (Fig. 1*E*) has been proposed to explain the responses of cortical neurons to first- and second-order stimuli (Zhou and Baker 1993; Mareschal and Baker 1999; Song and Baker 2007). The first stream consists of a conventional coarse spatial scale linear filter (F_0) selective for

orientation, direction of motion, and spatial frequency of luminance gratings. The second stream consists of a nonlinear FRF model (Fig. 1*F*) that can explain the responses of neurons to second-order stimuli such as contrast- and texture-defined boundaries (Chubb and Sperling 1988; Wilson 1999; Landy and Graham 2004). This FRF model is composed of two linear filtering stages that are connected by a nonlinearity (e.g., rectification). The first stage consists of small-scale spatial filters (F_1) that are selective for high spatial frequencies of the carrier. The outputs of these early filters are rectified and pooled by a coarse spatial scale late filter (F_2), which is selective for envelope orientation, direction of motion, and spatial frequency. Filters F_0 and F_2 have similar preferences for orientation and direction of motion, but spatial frequency selectivity is coarser for F_2 compared with F_0. Here, we explored whether the FRF model proposed to explain responses to contrast- and texture-defined boundaries could also explain the responses of area 18 neurons to motion-defined boundaries.

If motion-defined boundaries are processed by a common FRF-like mechanism, then neurons should show similar tuning properties for carrier and envelope of motion- and contrast-defined boundaries. In the processing of motion-defined boundaries by an FRF model, filter F_1 could act as local motion detectors whose outputs will be rectified and pooled by filter F_2. If the same F_1 filters are used for processing motion- and contrast-defined boundaries, then neurons should have similar carrier spatial frequency selectivity for both kinds of boundaries. Our results demonstrate that a given neuron is indeed selective for similar carrier spatial frequency for motion- and contrast-defined gratings (Fig. 2).

Such an FRF model could detect VM grating stimuli in two ways. The neuron could be responding to differences in the speeds of drifting carriers between adjacent half-cycles of VM gratings (region-based processing) and/or to the dynamic discontinuities (carriers in adjacent half-cycles moving in and out of phase with one another) along the boundaries (edge-based processing) similar to illusory contours (Song and Baker 2007). Since dynamic phase discontinuities are present in both uni- and bidirectional VM gratings, an FRF model could produce an edge-based response to both stimuli. For this model to respond in a region-based manner to unidirectional VM gratings, its early F_1 filters must respond differently to station-

ary and moving carriers. For bidirectional VM gratings, an FRF model will give a region-based response only if its early filters can distinguish between carriers drifting with equal speeds in opposite directions, which is possible only if the early filters are selective for motion direction.

We measured the temporal tuning properties of early filters by systematically varying the temporal frequency of a drifting carrier grating for contrast-defined boundary stimuli (Fig. 8). The neurons' responses were symmetric for both directions of carrier motion, suggesting that early filters of the FRF model are not direction selective. For most neurons, the response peaked when the carrier was held stationary and gradually declined with increasing carrier temporal frequencies. Since early filters of the FRF model are not direction selective, the FRF model would predict (Fig. 6*B*) symmetric carrier temporal frequency tuning for both directions of carrier motion for unidirectional VM gratings, which our results (Fig. 6, *C–H*) largely demonstrated. The model would also predict that responses to unidirectional VM gratings would be mediated by both edge-based processing (because of dynamic discontinuities) and region-based processing (because early filters give different responses to stationary and moving carrier). Responses to bidirectional VM gratings would be mediated by edge-based processing only and not by region-based processing (because early filters are not direction selective), as shown in Fig. 12.

To test these predictions about the mechanism, we measured envelope spatial frequency tuning for both uni- and bidirectional VM gratings and compared it with envelope spatial frequency tuning for ICs. ICs are thought to be detected in an edge-based manner (Wilson 1999; Song and Baker 2007), so if a VM grating is also detected in an edge-based manner it will show the same tuning for envelope spatial frequency as an IC. However, if a VM grating is detected by region-based processing [like contrast-defined boundaries (Song and Baker 2007)], it will be tuned to an envelope spatial frequency twice that of ICs, as there are two phase discontinuity edges in one envelope cycle of an IC. Our results (Fig. 11) from both neurons and model simulations showed that bidirectional VM grating responses are tuned to the same envelope spatial frequencies as ICs. However, unidirectional VM grating responses were tuned to spatial frequencies approximately twice the optimal for ICs. This result suggests that unidirectional gratings are detected by

Fig. 12. Schematic FRF model and its action on ICs and bidirectional and unidirectional VM gratings. The late filter (F_2) is shown superimposed on full-wave rectified responses of the early filters (F_1) for snapshot images of each stimulus, to show selectivity for envelope SF and orientation. Note the "edge-based processing" for ICs and bidirectional gratings and "region-based processing" for unidirectional gratings, as well as the corresponding difference in envelope SF selectivity.
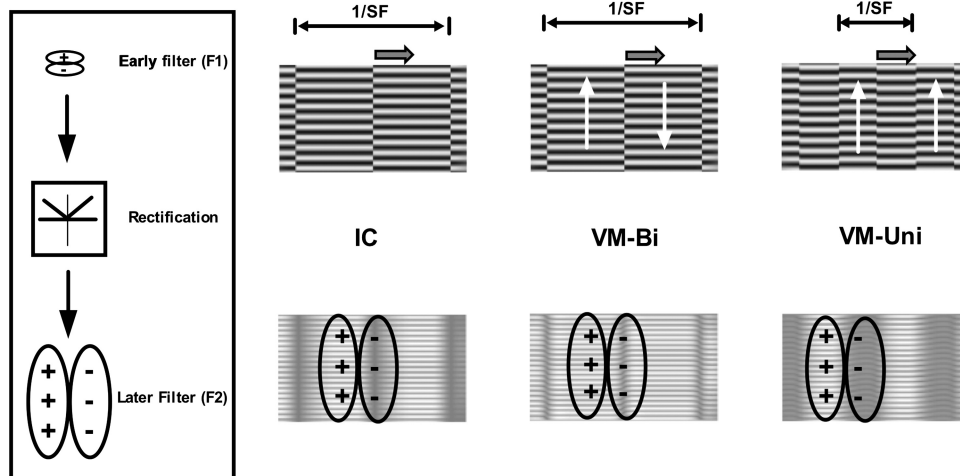
a mixture of both region-based and edge-based processing. In addition, our results (Fig. 10) showed that responses of neurons are stronger to unidirectional than to bidirectional gratings; this could be because unidirectional gratings are simultaneously detected by both region-based and edge-based processing, whereas bidirectional gratings are detected by edge-based processing only.

The results from our model simulations also predicted that neurons' FIs for carrier temporal frequency to uni- and bidirectional gratings would be different (Figs. 7*B* and 8*B*), which was demonstrated by the neurons' responses in Figs. 7 and 8. However, it should be noted that this model was not accurate in explaining all the details of individual neuron's responses, particularly the diversity of temporal responses (Figs. 6–8); to do so would require a more elaborate model architecture and additional model parameters, whose estimation would be beyond the aims and scope of this study. The purpose of this model was just to demonstrate, in a general way, how a simple FRF model could produce patterns of selectivity to different second-order stimuli that are similar to the neuronal data, particularly different carrier temporal frequency FIs to different stimuli and differing envelope spatial frequency selectivities.

The neural substrates for the elements of the FRF model are not known with certainty. It has been previously proposed that area 17 neurons could be the basis for the early filters (F_1) due to their selectivity for high spatial frequency and the orientation selectivity shown for the carrier of CM gratings, which seemed to rule out a subcortical substrate (Mareschal and Baker 1998). However, a recent study (Rosenberg et al. 2010) showed that LGN Y cells also respond selectively to CM gratings; most interestingly, the nonlinear subunits of Y cells exhibited carrier orientation tuning similar to that seen in area 18 neurons. These results suggest that nonlinear subunits of Y cells could provide the early filters (F_1), with subsequent cortical summation of Y cell afferents providing the envelope orientation and spatial frequency tuning (F_2) observed in area 18 neurons. Also consistent with this idea are the very good responses to quite high carrier temporal frequencies in both LGN Y cells (Rosenberg et al. 2010) and area 18 neurons (Fig. 8) (Rosenberg and Issa 2011), whereas area 17 neurons failed to respond at high temporal frequencies (Movshon et al. 1978). On the other hand, carrier spatial frequency tuning bandwidth is very broad in LGN Y cells compared with that in area 18 neurons (Rosenberg et al. 2010), so it is not yet clear to what extent the early filtering (F_1) might be accounted for at the geniculate level.

In summary, our results are consistent with the idea that these VM grating responses can be understood in terms of the same FRF model previously proposed for responses to CM and IC stimuli, suggesting a common neural mechanism for all these second-order stimuli.

Cue invariance. For the visual system to perform figure-ground segregation, it should be able to delineate an object from a background, which might be the same with respect to all cues except one, e.g., color. However, that object should also stand out if it appears against a different background with the same color but a different texture. To perform this task, information about presence of a particular cue is not important, but rather the contrast between cues that distinguish an object from its background is of primary importance, regardless of the nature of the cues. Thus, the visual system should be able to combine information across different cues to perform figure-ground segregation, i.e., the segmentation mechanism should be form-cue invariant (Albright 1992). This strategy of form-cue invariance is computationally economical and can help resolve perceptual ambiguities when multiple cues are present. In addition, it might be important for shape recognition and shape constancy.

Neurons in the early visual cortex have been previously shown to respond in a form-cue invariant manner to stimulus attributes such as orientation and motion direction of boundaries. Neurons in cat area 17 (Zhou and Baker 1993, 1996), cat area 18 (Zhou and Baker 1993, 1996; Mareschal and Baker 1998a, 1998b; Leventhal et al. 1998; Zhou et al. 2001; Song and Baker 2006, 2007; Tanaka and Ohzawa 2006), primate V1 (Chaudhuri and Albright 1997), and primate V2 (e.g., von der Heydt et al. 1984; von der Heydt and Peterhans 1989; Leventhal et al. 1998; Lui et al. 2005) have been shown to respond in a form-cue invariant manner to the orientation of luminance and nonluminance boundaries.

A long-standing concern has been the possibility that second-order responses might be mediated by simple early nonlinearities in the display device or the photoreceptors, or by luminance signals in the stimuli, without any implication of a specialized mechanism (e.g., FRF) to explain the form-cue invariance. However, the demonstration of carrier-tuned responses to stimuli with sine-wave grating carriers in previous studies (e.g., Zhou and Baker 1994; Mareschal and Baker 1998) as well as in the present study (Fig. 2) make such explanations seem very unlikely. One group failed to find carrier-tuned second-order-responsive neurons in cat area 18 and primate V2 (El-Shamayleh and Movshon 2011), but other laboratories have consistently replicated such tuned respones in cat area 18 (Rosenberg et al. 2010; Tanaka and Ohzawa 2006) and recently also in primate V2 (Li et al. 2011).

In this study, we demonstrated that neurons previously shown to selectively respond to luminance-, texture-, and contrast-defined boundaries can also display form-cue invariant responses to motion-defined boundaries. These neurons showed similar orientation selectivity for luminance- and motion-defined boundaries, but direction selectivity was weaker to motion-defined boundaries, similar to what has been previously found for contrast- and texture-defined boundaries (Song and Baker 2006, 2007). This form-cue invariant orientation tuning in the early visual cortex could be used by higher brain areas such as the MT, V4, and inferior temporal (IT) that have been reported to respond to motion-defined patterns in a form-cue invariant manner (Albright 1992; Mysore et al. 2006; Sary et al. 1993).

This study suggests that specific processing of motion-defined boundaries begins in early visual areas. Furthermore, it suggests that these boundaries are processed by a common nonlinear mechanism that also mediates response to other second-order stimuli, such as contrast-and texture-defined boundaries, and it could be the basis for form cue invariance to these stimuli.

REFERENCES

Adelson EH, Bergen JR. Temporal energy models for the perception of motion. *J Opt Soc Am* 2: 284–299, 1985.

Albright TD. Form-cue invariant motion processing in primate visual cortex. *Science* 255: 1141–1143, 1992.

Allard R, Faubert J. Double dissociation between first- and second-order processing. *Vision Res* 47: 1129–1141, 2007.

Baker CL, Mareschal I. Processing of second-order stimuli in the visual cortex. *Prog Brain Res* 134: 171–191, 2001.

Born RT, Tootell RBH. Segregation of global and local motion processing in primate middle temporal visual area. *Nature* 357: 497–499, 1992.

Born RT. Center-surround interactions in the middle temporal visual area of the owl monkey. *J Neurophysiol* 84: 2658–2669, 2000.

Brainard DH. The psychophysics toolbox. *Spat Vis* 10: 433–436, 1997.

Chaudhuri A, Albright TD. Neuronal responses to edges defined by luminance vs. temporal texture in macaque V1. *Vis Neurosci* 14: 949–962, 1997.

Chubb C, Sperling G. Drift balanced random stimuli: a general basis for studying non-Fourier motion perception. *J Optic Soc Am* 5: 1986–2007, 1988.

DeAngelis CG, Freeman RD, Ohzawa I. Length and width tuning of neurons in the cat's primary visual cortex. *J Neurophysiol* 71: 347–374, 1994.

Dupont P, De Bruyn B, Vandenberghe R, Rosier AM, Michiels J, Marchal G, Mortelmans L, Orban GA. The kinetic occipital region in human visual cortex. *Cereb Cortex,* 7: 283–292, 1997.

Efron B, Tibshirani B. *An Introduction to Bootstrap.* New York: Chapman & Hall, 1993.

El-Shamayleh Y, Movshon JA. Neuronal responses to texture-defined form in macaque visual area V2. *J Neurosci* 31: 8543–8555, 2011.

Fernald R, Chase R. An improved method for plotting retinal landmarks and focusing the eyes. *Vis Res* 11: 95–96, 1971.

Hubel DH, Wiesel TN. Receptive fields, binocular interaction and functional architecture in cat's visual cortex. *J Physiol* 160: 106–154, 1962.

Landy MS, Graham N. Visual perception of texture. In: *The Visual Neurosciences,* edited by Chalupa LM, Werner JS. Cambridge, MA: MIT Press, 2004, p. 1106–1118.

Larsson J, Heeger DJ. Two retinotopic visual areas in human lateral occipital cortex. *J Neurosci* 26: 13128–13142, 2006.

Larsson J, Heeger DJ, Landy MS. Orientation selectivity of motion-boundary responses in human visual cortex. *J Neurophysiol* 104: 2940–2950, 2010.

Ledgeway T, Smith AT. Evidence for separate motion-detecting mechanisms for first- and second-order motion in human vision. *Vis Res* 34: 2727–2740, 1994.

Leventhal AG, Wang Y, Schmolesky MT, Zhou Y. Neural correlates of boundary perception. *Vis Neurosci* 15: 1107–1118, 1998.

Li G, Wang Z, Yao Z, Yuan N, Talebi V, Tan J, Wang Y, Zhou Y, Baker CL Jr. *Form-Cue Invariant Second-Order Contrast Envelope Responses in Macaque V2.* Washington, DC: Society for Neuroscience Annual Meeting, 2011, Program No. 271.08.2011.

Lui LL, Bourne JA, Rosa MG. Single unit responses to kinetic stimuli in New World monkey area V2: physiological characteristics of cue-invariant neurons. *Exp Brain Res* 162: 100–108, 2005.

Marr D. *Vision.* San Francisco, CA: Freeman, 1982.

Marcar VL, Raiguel SE, Xiao D, Orban GA. Processing of kinetically defined boundaries in areas V1 and V2 of the macaque monkey. *J Neurophysiol* 84: 2786–2798, 2000.

Mareschal I, Baker CL. A cortical locus for the processing of contrast-defined contours. *Nat Neurosci* 1: 150–154, 1998a.

Mareschal I, Baker CL Jr. Temporal and spatial response to second-order stimuli in cat area 18. *J Neurophysiol* 80: 2811–2823, 1998b.

Mareschal I, Baker CL Jr. Cortical processing of second-order motion. *Vis Neurosci* 16: 527–540, 1999.

Marida KV. *Statistics of Directional Data.* New York: Academic Press, 1972.

Mather G, West S. Evidence for second-order motion detectors. *Vis Res* 33: 1109–1112, 1993.

Movshon JA, Thompson ID, Tolhurst DJ. Spatial and temporal contrast sensitivity of neurons in areas 17 and 18 of the cat's visual cortex. *J Physiol* 283: 101–120, 1978.

Mysore SG, Vogels R, Raiguel SE, Orban GA. Processing of kinetic boundaries in macaque V4. *J Neurophysiol* 95: 1864–1880, 2006.

Nikara T, Bishop PO, Pettigrew JD. Analysis of retinal correspondence by studying receptive fields of binocular single units in cat striate corte. *Exp Brain Res* 6: 353–372, 1968.

Nishida S, Ledgeway T, Edwards M. Dual multiple-scale processing for motion in the human visual system. *Vis Res* 37: 2685–2698, 1997.

Pelli DG. The VideoToolbox software for visual psychophysics: transforming numbers into movies. *Spat Vis* 10: 437–442, 1997.

Regan D. Orientation discrimination for objects defined by relative motion and objects defined by luminance contrast. *Vis Res* 29: 1389–1400, 1989.

Regan D, Hamstra SJ. Dissociation of orientation discrimination from form detection for motion-defined bars and luminance-defined bars: effects of dot lifetime and presentation duration. *Vis Res* 32: 1655–1666, 1992.

Reppas JB, Niyogi S, Dale AM, Sereno MI, Tootell RB. Representation of motion boundaries in retinotopic human visual cortical areas. *Nature* 388: 175–179, 1997.

Rogers B, Graham M. Motion parallax as an independent cue for depth perception. *Perception* 8: 125–134, 1979.

Rosenberg A, Husson TR, Issa NP. Subcortical representation of non-Fourier image features. *J Neurosci* 30: 1985–1993, 2010.

Rosenberg A, Issa NP. The Y cell visual pathway implements a demodulating nonlinearity. *Neuron* 71: 348–361, 2011.

Sary G, Vogels R, Orban GA. Cue-invariant shape selectivity of macaque inferior temporal neurons. *Science* 260: 995–997, 1993.

Sary G, Vogels R, Orban GA. Orientation discrimination of motion defined gratings. *Vis Res* 34: 1331–1334, 1994.

Sary G, Vogels R, Kovacs G, Orban GA. Responses of monkey inferior temporal neurons to luminance, motion and texture-defined gratings. *J Neurophysiol* 4: 1341–1354, 1995.

Scott-Samuel NE, Georgson MA. Does early non-linearity account for second-order motion? *Vis Res* 39: 2853–2865, 1999.

Sheth BR, Sharma J, Rao SC, Sur M. Orientation maps of subjective contours in visual cortex. *Science* 274: 2110–2115, 1996.

Shen Z, Xu W, Li C. Cue-invariant detection of centre-surround discontinuity by V1 neurons in awake macaque monkey. *J Physiol* 538: 581–592, 2007.

Skottun BC. Illusory contours and linear filters. *Exp Brain Res* 100: 360–364, 1994.

Song Y, Baker CL Jr. Neural mechanisms mediating responses to abutting gratings: luminance edges vs. illusory contours. *Vis Neurosci* 23: 181–199, 2006.

Song Y, Baker CL Jr. Neuronal response to texture- and contrast-defined boundaries in early visual cortex. *Vis Neurosci* 24: 65–77, 2007.

Tanaka H, Ohzawa I. Neural basis for stereopsis from second-order contrast cues. *J Neurosci* 26: 4370–4382, 2006.

Tusa RJ, Rosenquist AC, Palmer LA. Retinotopic organization of areas 18 and 19 in the cat. *J Comp Neurol* 185: 657–678, 1979.

Tyler CW, Likova LT, Kontsevich LL, Wade AR. The specificity of cortical region KO to depth structure. *Neuroimage* 30: 228–238, 2006.

Van Oostende S, Sunaert S, Van Hecke P, Marchal G, Orban GA. The kinetic occipital (KO) region in man: an fMRI study. *Cereb Cortex* 7: 690–701, 1997.

von der Heydt R, Peterhans E, Baumgartner G. Illusory contours and cortical neuron responses. *Science* 244: 1260–1262, 1984.

von der Heydt R, Peterhans E. Mechanisms of contour perception in monkey visual cortex I Lines of pattern discontinuity. *J Neurosci* 9: 1731–1748, 1989.

Watson AB, Ahumada AJ. Model of human visual-motion sensing. *J Opt Am* 2: 322–342, 1985.

Wilson H. Non-Fourier cortical processes in texture, form, and motion perception. *Cereb Cortex* 13: 445–477, 1999.

Zeki S, Perry RJ, Bartels A. The Processing of kinetic contours in the brain. *Cereb Cortex* 13: 189–202, 2003.

Zhan CA, Baker CL Jr. Boundary cue invariance in cortical orientation maps. *Cereb Cortex* 16: 896–906, 2006.

Zhou YF, Jia F, Tao HY, Shou TD. The responses to illusory contours of neurons in cortex areas 17 and 18 of the cats. *C-Life Sci* 44: 136–145, 2001.

Zhou YX, Baker CL Jr. A processing stream in mammalian visual cortex neurons for non-Fourier responses. *Science* 261: 98–101, 1993.

Zhou YX, Baker CL Jr. Envelope-responsive neurons in areas 17 and 18 of cat. *J Neurophysiol* 72: 2134–2150, 1994.

Zhou YX, Baker CL Jr. Spatial properties of envelope-responsive cells in area 17 and 18 neurons of the cat. *J Neurophysiol* 75: 1038–1050, 1996.